

Improved Angle-of-Arrival Estimation of Narrow Gaussian Beams for Mobile FSO Platforms

MING-CHENG TSAI , Graduate Student Member, IEEE
King Abdullah University of Science and Technology, Thuwal, Kingdom of Saudi Arabia

MUHAMMAD SALMAN BASHIR , Senior Member, IEEE
University of Huddersfield, Huddersfield, U.K.

MOHAMED-SLIM ALOUINI , Fellow, IEEE
King Abdullah University of Science and Technology, Thuwal, Kingdom of Saudi Arabia

Due to the narrow beamwidths of laser Gaussian beams, accurate tracking of laser beam's angle of arrival is an important problem in mobile free-space optical communications. In most optical receivers today, fine tracking of angle of arrival involves estimating the location of the focused beam spot projected onto a focal plane array. However, for very thin Gaussian beams, both the location, as well as the energy of the spot varies considerably with the variation of angle of arrival. In this study, we have analyzed the relationship between the angle of arrival and the energy of laser spot on the focal plane. We then exploited this relationship to enhance the angle-of-arrival estimation performance of our proposed receiver that takes into account both the location as well as the energy of the laser spot while estimating the angle of arrival. The derived Cramér–Rao bounds indicate that the system performance can be enhanced significantly for narrow Gaussian beams when both the spot location and energy are exploited for angle-of-arrival estimation.

Manuscript received 29 July 2023; revised 3 November 2023; accepted 2 January 2024. Date of publication 19 February 2024; date of current version 11 June 2024.

DOI. No. 10.1109/TAES.2024.3367286

Refereeing of this contribution was handled by J. Choi.

This work was supported by the KAUST Office of Sponsored Research.

Authors' addresses: Ming-Cheng Tsai and Mohamed-Slim Alouini are with the King Abdullah University of Science and Technology, Thuwal 23955-6900, Kingdom of Saudi Arabia, E-mail: (mingcheng.tsai@kaust.edu.sa; slim.alouini@kaust.edu.sa); Muhammad Salman Bashir is with the University of Huddersfield, HD1 3DH Huddersfield, U.K., E-mail: (m.bashir@hud.ac.uk). (*Corresponding author: Muhammad Salman Bashir.*)

0018-9251 © 2024 IEEE

I. INTRODUCTION

Due to the availability of large unregulated spectrum in the optical domain of electromagnetic waves, free-space optics (FSO)—also known as optical wireless or laser communications—is an important candidate for supporting high data-rates in the 6G and beyond terrestrial and nonterrestrial wireless networks [1]. FSO has been deployed successfully in nonterrestrial networks, such as high speed communications between satellites in low-Earth orbit (LEO), medium-Earth orbit (MEO), geosynchronous-equatorial orbit (GEO), and high-Earth orbit (HEO). FSO has also found considerable use in hybrid space-terrestrial networks [2]. The National Aeronautics and Space Administration (NASA) demonstrated a downlink data rate up to 622 Mbps from the Moon to the Earth in the Aerospace Corporation's Optical Communication and Sensor Demonstration in 2017 [3]. In addition, NASA's TeraByte InfraRed Delivery system promises data rate transfers up to 200 Gbps from a CubeSat in LEO to a ground station using laser communications [3], [4].

The angular beamwidth ϕ of laser Gaussian beam (in the paraxial case) is proportional to λ/π [5]. This implies that it is not uncommon to achieve angular beamwidths up to a fraction of a milliradian with moderate size transmit apertures. Narrow beamwidths allow squeezing of energy into a narrow cone that leads to increased transmit energy density and higher signal-to-noise ratio at the receiver. Narrow beamwidths can also help in realizing transfer of energy, as well as data simultaneously, a concept known as *simultaneous lightwave information and power transfer* [6], [7], [8], [9], [10], [11]. Moreover, narrow beamwidths of laser signals minimize interference with neighboring terminals and endow FSO terminals with security and antijamming advantages unavailable to conventional RF systems [12].

However, communications with narrow beams is not easy, more so in the case of mobile FSO terminals. FSO terminals need to first acquire the narrow beam laser signal (a process known as *acquisition*) [13], [14] before the link is setup. When acquisition is achieved successfully, mobile terminals are required to maintain link alignment by tracking the angle of arrival of the incoming beam. Therefore, acquisition and tracking subsystems (comprising of hardware as well as algorithms) form important blocks of any modern optical receiver, and much effort has been devoted in recent past to improving the acquisition and tracking performance of FSO communication systems [15].

Majority of the lasers emit beams with a Gaussian intensity profile [16]. In this case, the laser's optical resonator is said to be operating in the *fundamental transverse mode* or TEM_{00} mode. The Gaussian beam preserves its profile at any point along the beam axis [17]. Moreover, the Gaussian profile is also preserved as the beam passes through lens [17], [18]. Also, single-mode fibers emit laser beams whose profile is closely approximated by a Gaussian distribution. All these attributes render Gaussian beams

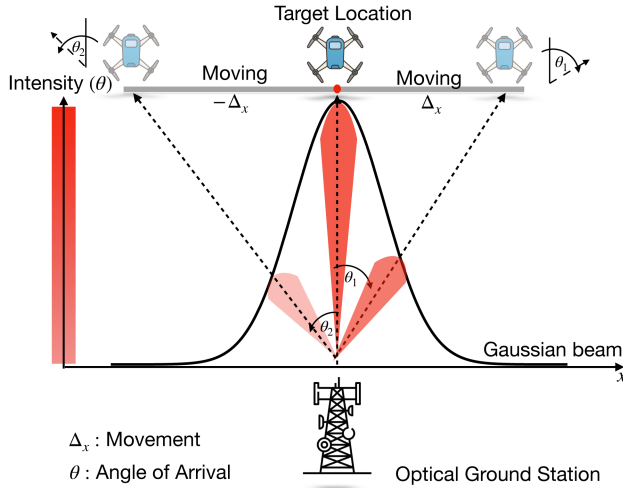


Fig. 1. This figure shows the change in the signal energy received by the UAV as it moves away from the center of the Gaussian beam and creates a nonzero angle-of-arrival θ with respect to the ground station's angle of transmission. In this figure, $\theta_2 > \theta_1$.

important and the most widely used intensity model in free-space optical communications.

A. Motivation of Current Study

Due to narrow beamwidth of laser beams, free-space optical terminals have to track the incoming beam's angle of arrival continuously to maintain sufficient signal-to-noise ratio at the receiving terminal. This fact is illustrated in Fig. 1 which shows a mobile UAV with respect to a stationary optical ground station (OGS). Depending on the angle θ , the UAV makes with the OGS's direction of transmission, the received signal energy at the UAV diminishes depending on the value of θ and the angular beamwidth of the transmitted beam. Fig. 2 highlights the decay in received energy with the nonzero angle of arrival. In the old position, the receiving terminal is aligned with the transmitter (the receiver aperture normal is at the same angle as the incoming beam). In this position, the receiver receives maximum signal energy since the Gaussian beam packs the highest energy density at the center of the beam. However, when the terminal moves to the new position, the receive aperture normal makes an angle $|\theta| > 0$ with the incoming beam. We define θ as the *angle of arrival* of the laser beam with respect to the direction of the normal to receiver aperture. In order to maintain the same energy as before, the receiver needs to track this nonzero angle of arrival and transmit this information over to the transmitter so that the transmitter can point to the new receiver location in order to maximize the signal-to-noise ratio.

A number of studies on laser beam tracking [15], [19], [20], [21], [22], [23] indicates that the angle of arrival of an incoming laser beam is estimated or tracked based on the location of a focused spot on a quad detector or an array of detectors in the focal plane. In a 1-D plane, the incoming beam's angle of arrival causes a deviation of the spot position from the center of the array according to the

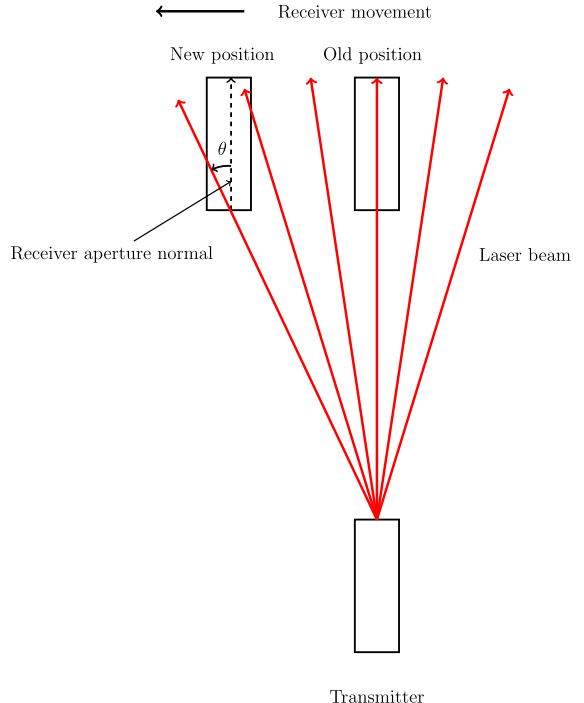


Fig. 2. Change in angle of arrival with receiver movement.

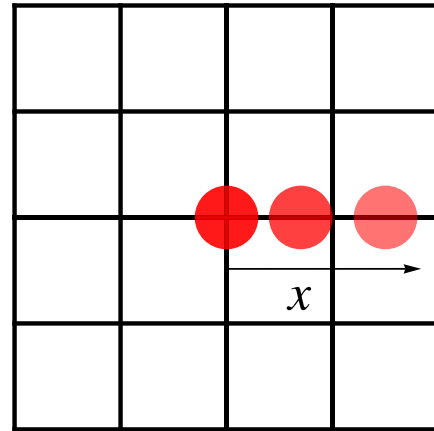


Fig. 3. Spot energy decays as it moves away from the center of the detector array.

relationship [24]

$$d = F \sin(\theta) \quad (1)$$

where d is the (1-D) Euclidean distance from the center of the array, F is the focal length of the receiver lens, and θ is the angle of arrival. In this scenario, if we estimate the deviation d , we can infer angle-of-arrival θ . However, as shown in Fig. 3, the information of angle of arrival is also captured in the energy or brightness of the spot on focal plane. A nonzero angle of arrival causes not only the deviation in position of spot but also causes the energy of the spot to diminish. This phenomenon is captured by the dark red spot closer to center of the array and the light red spot further away from the center. The variation in spot energy as a function of angle of arrival can be exploited further to enhance the tracking performance of the receiver. We

note that the variation of spot energy as a function of angle-of-arrival θ is highly dependent on the angular beamwidth (denoted by ϕ) of the laser beam: a highly narrow beam (small ϕ) leads to sharp variations of energy even for small values of angle of arrival, and incorporating the spot energy as an additional measurement will realize a more accurate angle-of-arrival tracking subsystem in the optical receiver.

The state-of-the-art conventional tracking systems take into account only one parameter for the estimation of angle-of-arrival θ : the spot location on the focal plane array. However, since the spot energy also contains information about the angle of arrival, a tracking system that takes into account both the spot location, as well as the spot energy as observations will yield a better tracking performance compared to a system that only rely on spot location as their observations. Motivated by this fact, we show, in this study, that the angle-of-arrival estimation performance improves considerably—especially for small angle of arrival—if we take the spot energy into account in addition to spot location on the focal plane. We expect that the narrower the beam is, the greater the difference in the tracking performance of the two systems.

B. Literature Review

In this section, we discuss a number of technical papers on pointing, acquisition, and tracking for FSO applications. Here, we will focus mainly on angle-of-arrival estimation techniques from a systems and signal processing perspective. However, see [15] for a comprehensive survey on pointing, acquisition, and tracking for FSO.

We now consider angle-of-arrival estimation based on spot location in the focal plane of a free-space optical receiver. The study [20] examined three angle-of-arrival estimation techniques based on centroid, template-matching, and maximum likelihood estimators. The observations for these estimators are the outputs of the individual detectors of the focal plane array. The study [21] built on [20] to analyze Bayesian filters—such as Kalman filter and particle filter—for tracking small changes in the spot location on the focal plane. The authors in [22] considered the impact of error in angle-of-arrival tracking on the pulse position modulation (PPM) symbol detection performance of the receiver. The study [23] derived Cramér–Rao lower bounds (CRLB) for the angle-of-arrival estimation with detector arrays. In this study, the authors examine the effect of spot radius on CRLB and discuss decision-aided tracking schemes for maximal ratio combining receivers. All of these aforementioned studies consider a Poisson channel that is more relevant in deep space communications context. In contrast, the authors in [19], [25], and [26] considered beam tracking for a Gaussian channel. In these studies, the authors considered spot position sensing algorithms with the help of a detector array in the focal plane. Specifically, the authors in [26] considered optimal power allocation between beam tracking and symbol detection channels in order to minimize the bit error rate of the Gaussian optical channel. The experimental study [27] estimated the angle of

arrival based on angle-dependent properties of interference optical filters.

We now discuss a few important studies on pointing error in FSO. The authors in [28] considered optimization of the outage capacity of an optical link in presence of pointing errors, whereas the study [29] considers adaptive beam control techniques to mitigate the effect of pointing error. Bekkali et al. [30] devised intelligent lens-based optical-beam stabilization (OBS) by employing miniature and cost-effective three-axis voice-coil motors to minimize pointing error for a reliable fiber-to-fiber FSO link. The authors in [31] mitigated the effect of pointing error by optimizing the locations of hovering unmanned aerial vehicles (UAV) in a serial FSO link. The article [32] proposes metalenses integrated receiver for FSO that is more robust against angle-of-arrival fluctuations compared to a traditional FSO receiver. The effect of angle-of-arrival fluctuations on the mixing efficiency of heterodyne detection in an optical receiver is investigated in detail in [33].

For acquisition of FSO terminals, the authors in [13] discussed optimization problems for the spiral scanning approach, where the authors consider optimizing the beam footprint in order to maximize acquisition performance. In their study, they use the mean acquisition time and the complementary cumulative distribution function of acquisition time as performance metrics. The study [14]—that builds on [13]—proposes adaptive spiral scanning schemes for enhancing the acquisition performance of FSO terminals in photon-starved regimes. For this approach, the scanning terminal searches region of higher probability of receiver location more often than low probability regions in order to reduce acquisition time. Heyou et al. [34] considered acquisition of mobile FSO terminals in a GPS-denied environment. In this work, the authors maximize the acquisition performance of a LiDAR-assisted mobile FSO platform by optimal allocation of power between lidar and optical transmitter assemblies colocated at the OGS.

For readers interested in communications with an array of detectors in free-space optical communications, [23], [35], [36], [37], and [38] provide comprehensive introduction on the subject. The authors in [35] showed that the error probability performance of maximal ratio combining array receiver improves monotonically with the number of detectors in the array for a fixed array size. The authors in [39] proposed time synchronization algorithms of PPM symbols based on an array of detectors. In another study, the authors in [40] discussed multiple-input-single-output FSO communications based on an array of detectors. Tsai et al. [41] analyzed the diversity techniques—such as equal gain combining and maximal ratio combining—based on the outputs of detectors of an array receiver to maximize system performance.

C. Contributions of This Study

The state-of-the-art tracking systems considered in literature review operate on the information furnished by location of the focal spot to infer the angle of arrival. However,

in the current study, we have argued that the spot energy is also a function of the angle of arrival, and estimation algorithms operating on the spot energy, as well as spot location would yield superior performance compared to algorithms that only take spot location into account. To substantiate our argument, we derived CRLB of angle-of-arrival θ for quite a few scenarios, and we were able to show that the Cramér–Rao bounds based on both spot location as well as energy are lower in magnitude compared to the Cramér–Rao bounds based exclusively on spot location for all values of θ . To generate the Cramér–Rao bounds, the first important step is to establish the relationship between the beam intensity captured by the receiver telescope and the angle of arrival. In this study, we were able to show that the beam intensity and the angle of arrival of a Gaussian beam are related through the *Lambert W* function, as indicated by (14).

The maximum likelihood estimator of the angle of arrival is derived in this study along with a mean-square error performance comparison with respect to the the Cramér–Rao bounds. The effect of beamwidth uncertainty—where the actual beamwidth of a Gaussian beam is not the same as the beamwidth assumed in the model—on the performance of maximum likelihood estimator is also analyzed.

From this study, we infer some important results. For instance, for the same beam power, a smaller beamwidth will lead to more information (about θ) in spot energy and a greater improvement in performance compared to wider beamwidths for values of θ close to zero. However, as θ becomes large, narrow beamwidth signals will lose energy rather quickly compared to wider beamwidths, and in order to estimate large θ , wider beamwidth laser signals will outperform signals with narrow beamwidth. In the latter part of the article, we analyze the Cramér–Rao bounds for optical channels suffering from pointing error, where the (Gaussian distributed) pointing error is treated an additional source of noise in the receiver.

This study will find significant application in mobile platform communications where the effect of atmospheric turbulence (on signal energy) is not significant. These include satellite-to-satellite communications in space, communications between high altitude platforms in stratosphere, short distance optical wireless channels, such as vehicle-to-vehicle channels, and indoor optical wireless communications based on infrared spectrum. Almost all of these channels will find widespread applications in 6G and beyond wireless communications standards [42]. We believe that the results of our study will lead to an efficient laser beam tracking system for mobile FSO terminals that will help realize tens of Tbps-level speeds with super-thin, narrow Gaussian beams.

D. Article Organization

The rest of this article is organized as follows. Section II introduces the system model wherein we derive the relationship between the Gaussian beam energy and the angle of arrival. Section III deals with the derivation of CRLB of the angle-of-arrival θ . In this section, we consider the

CRLB for two scenarios: 1) for the specific scenario where the channel suffers only from Gaussian noise and 2) the more general case that includes both Gaussian noise and pointing error. The model mismatch problem—where the actual beamwidth of Gaussian beam is not the same as the one assumed in our model—is discussed in Section V. In this section, the mean-square error of the maximum likelihood estimator is compared with the CRLB curves and the performance of the maximum likelihood estimator is evaluated under beamwidth uncertainty. We highlight and discuss experimental results in Section VI. Finally, Section VII concludes this article.

II. RELATIONSHIP BETWEEN BEAM ENERGY AND ANGLE OF ARRIVAL

As highlighted before, a major goal of this study is to estimate the angle of arrival of a Gaussian beam at the receiver. As a first (important) step, we establish the variation of Gaussian beam energy at the receiver as a function of angle of arrival. To achieve this, we first define the Gaussian beam intensity as a function of distance from the beam center through the following relationship:

$$y(x) = \frac{I_0}{\sqrt{2\pi w(L)^2}} \exp\left(-\frac{x^2}{2w^2(L)}\right) \quad (2)$$

where y denotes the intensity of Gaussian beam in Watts/m². Here, we have assumed—without loss of generality—that the beam center lies at the origin. The quantity I_0 is the total power in the transmitted beam measured in Watts. The factor x represents the (1-D) distance from the beam center in a plane perpendicular to direction of beam propagation. For a Gaussian beam, the beam radius $w(L)$ evolves with distance L according to the relationship [1]

$$w(L) = w_0 \sqrt{1 + \left(\frac{\lambda L}{\pi w_0^2}\right)^2} \quad (3)$$

where λ is the wavelength of light signal and w_0 is known as the *beam waist*. When L is large, we have that

$$\begin{aligned} w(L) &= w_0 \sqrt{1 + \left(\frac{\lambda L}{\pi w_0^2}\right)^2} \approx w_0 \sqrt{\left(\frac{\lambda L}{\pi w_0^2}\right)^2} \\ &= \frac{\lambda}{\pi w_0} L. \end{aligned} \quad (4)$$

In (4), the quantity $\lambda/\pi w_0$ is termed as the half-angle *beamwidth*. For the sake of compactness, we will use the notation

$$\phi := \frac{\lambda}{\pi w_0} \quad (5)$$

to denote the angular beamwidth in radians. The expression of the Gaussian beam in terms of ϕ is reproduced as follows:

$$y(x) = \frac{I_0}{\sqrt{2\pi(L\phi)^2}} \exp\left(-\frac{x^2}{2(L\phi)^2}\right). \quad (6)$$

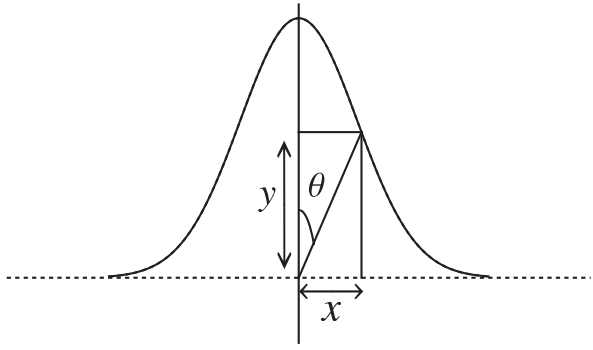


Fig. 4. Relationship between the Gaussian beam amplitude y , the angle-of-arrival θ , and deviation along x -axis.

As shown in Fig. 4, the Gaussian intensity y as a function of angle-of-arrival θ and deviation along x -axis is

$$y = \frac{x}{\tan(\theta)}. \quad (7)$$

By inserting $x = y \tan(\theta)$ into (6), we have that

$$y = \frac{I_0}{\sqrt{2\pi(L\phi)^2}} \exp\left(-\frac{y^2 \tan^2(\theta)}{2(L\phi)^2}\right) \quad (8)$$

$$\Rightarrow y \exp\left(\frac{y^2 \tan^2(\theta)}{2(L\phi)^2}\right) = \frac{I_0}{\sqrt{2\pi(L\phi)^2}}. \quad (9)$$

Squaring both sides of (9) and then multiplying both sides of (9) by $\frac{\tan^2(\theta)}{(L\phi)^2}$, we obtain,

$$\frac{y^2 \tan^2(\theta)}{(L\phi)^2} \exp\left(\frac{y^2 \tan^2(\theta)}{(L\phi)^2}\right) = \frac{I_0^2 \tan^2(\theta)}{2\pi(L\phi)^4}. \quad (10)$$

Here, we first note the property of *Lambert W* function that for any functions f and g , $f = g \exp(g) \Rightarrow g = W(f)$. Applying this property to (10), we have that

$$\frac{y^2 \tan^2(\theta)}{(L\phi)^2} = W\left(\frac{I_0^2 \tan^2(\theta)}{2\pi(L\phi)^4}\right) \quad (11)$$

$$\Rightarrow y = \frac{L\phi}{\tan(\theta)} \sqrt{W\left(\frac{I_0^2 \tan^2(\theta)}{2\pi(L\phi)^4}\right)}. \quad (12)$$

Finally, we note that

$$x = y \tan(\theta) \Rightarrow x = L\phi \sqrt{W\left(\frac{I_0^2 \tan^2(\theta)}{2\pi(L\phi)^4}\right)}. \quad (13)$$

Substituting the expression of x in (13) into (6), we obtain a mathematically tractable expression of intensity y in terms of angle-of-arrival θ as

$$y = \frac{I_0}{\sqrt{2\pi(L\phi)^2}} \exp\left(-\frac{1}{2}W\left(\frac{I_0^2 \tan^2(\theta)}{2\pi L^4 \phi^4}\right)\right) \cdot \mathbb{1}_{(-\frac{\pi}{2}, \frac{\pi}{2})}(\theta) \quad (14)$$

where $\mathbb{1}_A(x)$ represents the *indicator* function that is equal to unity whenever $x \in A$ for any measurable set A and zero otherwise.

Fig. 5 highlights the relationship between intensity y and the angle-of-arrival θ .

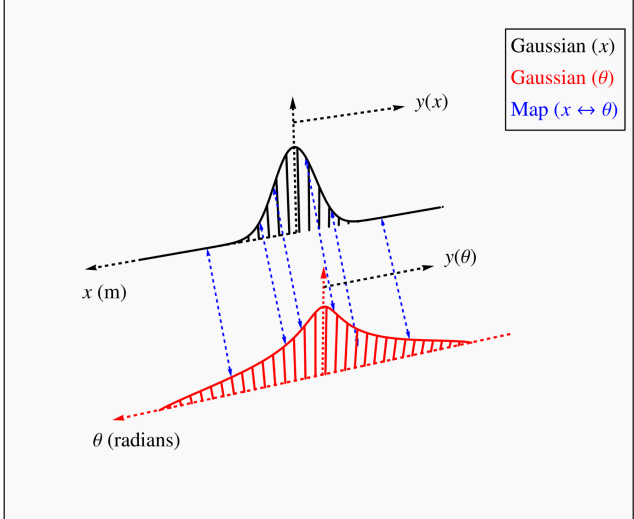
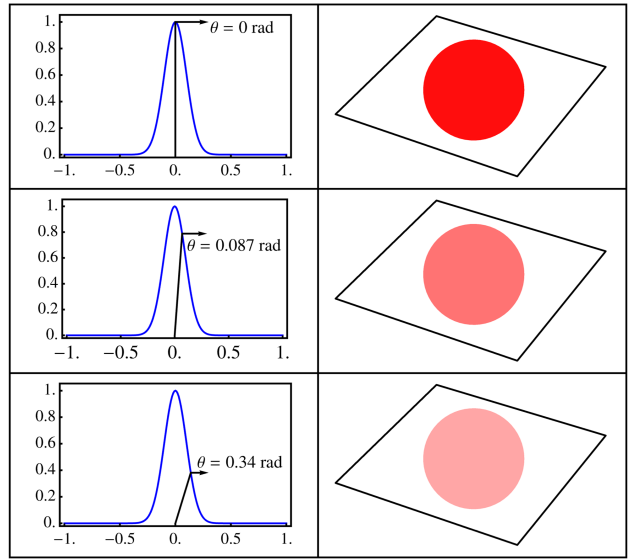


Fig. 5. Illustration of power variation in Gaussian beam with respect to the angle-of-arrival θ . The top figure represents the beam intensity variation with respect to angle θ . The bottom figure shows the intensity variation translation from the Gaussian (as a function of distance x) to the non-Gaussian distribution (with respect to angle θ).

III. CRAMÉR–RAO LOWER BOUND OF ANGLE OF ARRIVAL

In this section, we derive the Cramér–Rao bounds for the angle-of-arrival θ . For the sake of simplicity, we assume a 1-D array of detectors in the focal plane where the signal image is captured. In this scenario, the peak intensity—captured by the receiver telescope lens and projected onto a focal plane array—is given by the expression

$$\Lambda_0(\theta) = \frac{I_0}{\sqrt{2\pi(L\phi)^2}} \exp\left(-\frac{1}{2}W\left(\frac{I_0^2 \tan^2(\theta)}{2\pi L^4 \phi^4}\right)\right) \pi a^2 \quad (15)$$

where ϕ is the beamwidth in radians, L is the link distance in meters, I_0 is the peak (received signal) intensity impinging on the receive aperture and a is the receive telescope radius

in meters. Here, we have assumed that the beam footprint $\pi(L\phi)^2 \gg \pi a^2$. The signal intensity captured on the focal plane array is modeled by a (1-D) Gaussian distribution as

$$\Lambda_s(\theta) = \frac{\Lambda_0(\theta)}{\sqrt{2\pi\rho^2}} \exp\left(-\frac{(x - x_0(\theta))^2}{2\rho^2}\right) \cdot \mathbb{1}_{\mathcal{A}}(x) \quad (16)$$

where \mathcal{A} is the region of the square array, ρ is the spot size on the focal plane, and x_0 is the location of spot center on the 1-D array. Here, the center of the array is fixed at origin. The deviation x_0 of the spot center location on the array is related to the angle of arrival as

$$x_0(\theta) = F \sin(\theta) \quad (17)$$

where F is the focal length of receiver telescope lens in meters. We note that Λ_s in (16) is a function of angle-of-arrival θ due to dependence on the energy $\Lambda_0(\theta)$ of the spot as well as the location $x_0(\theta)$ of spot center on the focal plane array.

The output of thermal-noise (modeled by Gaussian distribution) limited array is

$$\mathbf{Y} = \boldsymbol{\Lambda} + \mathbf{X} \quad (18)$$

where \mathbf{Y} is $M \times 1$ output vector, $\boldsymbol{\Lambda}$ is $M \times 1$ signal vector, and \mathbf{X} is an $M \times 1$ noise vector. Here,

$$\mathbf{Y} = \begin{bmatrix} Y_0 & Y_1 & \dots & Y_{M-1} \end{bmatrix}^T \quad (19)$$

$$\boldsymbol{\Lambda} = \begin{bmatrix} \Lambda_0 & \Lambda_1 & \dots & \Lambda_{M-1} \end{bmatrix}^T \quad (20)$$

$$\mathbf{X} = \begin{bmatrix} X_0 & X_1 & \dots & X_{M-1} \end{bmatrix}^T \quad (21)$$

where Y_m is the output of the m th element of the array

$$Y_m = \Lambda_m + X_m, \quad m = 0, 1, \dots, M-1. \quad (22)$$

In (22),

$$\Lambda_m(\theta) := \int_{A_m} \Lambda_s(\theta) dx \quad (23)$$

$$= \frac{\Lambda_0(\theta)}{\sqrt{2\pi\rho^2}} \int_{A_m} \exp\left(-\frac{(x - x_0(\theta))^2}{2\rho^2}\right) dx \quad (24)$$

is the signal output of the m th detector of the array. Here, A_m is the region of the m th detector. The factor N_m represents a Gaussian random variable that models thermal noise of the m th detector. Here, $X_m \sim \mathcal{N}(0, \sigma_n^2)$ for all m and $X_m \perp X_j$ for positive integers m and j such that $m \neq j, 0 \leq m, j \leq M-1$. The quantity σ_n^2 is the thermal noise variance.

The log-likelihood of a single observation is described by

$$p(Y_m|\theta) = \frac{1}{\sqrt{2\pi\sigma_n^2}} \exp\left(-\frac{(Y_m - \Lambda_m(\theta))^2}{2\sigma_n^2}\right) \quad (25)$$

$$\ln p(Y_m|\theta) = -\ln\left(\sqrt{2\pi\sigma_n^2}\right) - \frac{(Y_m - \Lambda_m(\theta))^2}{2\sigma_n^2} \quad (26)$$

$$\ln p(\mathbf{Y}|\theta) = -M \ln\left(\sqrt{2\pi\sigma_n^2}\right) - \sum_{m=0}^{M-1} \frac{(Y_m - \Lambda_m(\theta))^2}{2\sigma_n^2}. \quad (27)$$

Taking the second derivative of the log-likelihood function with respect to θ , we obtain

$$\frac{\partial^2 \ln p(\mathbf{Y}|\theta)}{\partial \theta^2} = \sum_{m=0}^{M-1} \left(\frac{\Lambda_m''(\theta)(Y_m - \Lambda_m(\theta))}{\sigma_n^2} - \frac{(\Lambda_m'(\theta))^2}{\sigma_n^2} \right) \quad (28)$$

and the Fisher information of θ in random vector \mathbf{Y} is

$$-\mathbb{E}\left[\frac{\partial^2 \ln p(\mathbf{Y}|\theta)}{\partial \theta^2}\right] = \frac{1}{\sigma_n^2} \sum_{m=0}^{M-1} (\Lambda_m'(\theta))^2. \quad (29)$$

We now analyze the Fisher information of θ given in (29). After a few steps, it can be shown that Λ_m' [see the expression of Λ_m in (24)] can be decomposed into two terms α_m and β_m as

$$\Lambda_m'(\theta) = \alpha_m + \beta_m \quad (30)$$

where

$$\alpha_m := \frac{\Lambda_0'}{\sqrt{2\pi\rho^2}} \int_{A_m} \exp\left(-\frac{(x - x_0)^2}{2\rho^2}\right) dx \quad (31)$$

$$\beta_m := \frac{\Lambda_0 x_0'}{\sqrt{2\pi\rho^3}} \int_{A_m} \exp\left(-\frac{(x - x_0)^2}{2\rho^2}\right) (x - x_0) dx. \quad (32)$$

Here, we highlight that the factor β_m corresponds to the information of θ provided by spot location in the focal plane, whereas α_m corresponds to the information provided by spot energy.

After a number of mathematical manipulations, the derivative of Λ_0 , as a function of θ , is shown to be

$$\Lambda_0'(\theta) = -\frac{I_0(\pi a^2) \csc(\theta) \sec(\theta) e^{-\frac{1}{2}W\left(\frac{l_0^2 \tan^2(\theta)}{2L^4\phi^4}\right)} W\left(\frac{l_0^2 \tan^2(\theta)}{2L^4\phi^4}\right)}{\sqrt{2\pi} \sqrt{L^2\phi^2} \left(W\left(\frac{l_0^2 \tan^2(\theta)}{2L^4\phi^4}\right) + 1\right)}. \quad (33)$$

Moreover,

$$x_0'(\theta) = F \cos(\theta). \quad (34)$$

By substituting expression of Λ_0' and x_0' into (30), we obtain the Fisher information of θ from (29). The final form of the Fisher information (in terms of α_m and β_m) is

$$\begin{aligned} -\mathbb{E}\left[\frac{\partial^2 \ln p(\mathbf{Y}|\theta)}{\partial \theta^2}\right] &= \frac{1}{\sigma_n^2} \sum_{m=0}^{M-1} (\alpha_m + \beta_m)^2 \\ &= \frac{1}{\sigma_n^2} \sum_{m=0}^{M-1} \beta_m^2 + \frac{1}{\sigma_n^2} \sum_{m=0}^{M-1} \alpha_m^2 + \frac{1}{\sigma_n^2} \sum_{m=0}^{M-1} 2\alpha_m\beta_m. \end{aligned} \quad (35)$$

In (35), the first summation term on the right-hand side (containing β_m 's) corresponds to the Fisher information of θ based solely on the spot location in the focal plane, whereas the second and third summation terms comprise additional Fisher information when spot energy is considered as an extra observation in addition to spot location. The CRLB of θ can be reached by taking the inverse of the Fisher information

$$\text{CRLB}(\theta) = \frac{\sigma_n^2}{\sum_{m=0}^{M-1} (\alpha_m + \beta_m)^2}. \quad (36)$$

IV. CRAMÉR–RAO BOUNDS FOR GENERAL RECEIVER (THERMAL NOISE AND POINTING ERROR)

For the general receiver that suffers both from thermal noise and pointing error, the energy captured by receiver lens fluctuates as

$$\Lambda_0(\theta + \Theta_p) = \frac{I_0(\pi a^2)}{\sqrt{2\pi(L\phi)^2}} \exp\left(-\frac{1}{2}W\left(\frac{I_0^2 \tan^2(\theta + \Theta_p)}{2\pi L^4 \phi^4}\right)\right) \quad (37)$$

where Θ_p represents the *angular pointing error*. We assume that the pointing error is distributed as a Gaussian random variable: $\Theta_p \sim \mathcal{N}(0, \sigma_p^2)$, where σ_p^2 captures the angular pointing error variance. In addition to random fluctuation in spot energy Λ_0 , the angular pointing error also causes random fluctuations in spot center position on the array according to the relationship

$$x_0(\theta + \Theta_p) = F \sin(\theta + \Theta_p). \quad (38)$$

When pointing error variance σ_p^2 is close to zero, we have an approximate result for (38) based on the fact that $\cos(z) \approx 1$ and $\sin(z) \approx z$ for small z . The approximate result is,

$$x_0(\theta + \Theta_p) \approx F \sin(\theta) + F \cos(\theta)\Theta_p. \quad (39)$$

If the pointing error is small, then an approximate relationship for spot energy in (37) also holds through the Taylor Series expansion:

$$\Lambda_0(\theta + \Theta_p) \approx \Lambda_0(\theta) + \Lambda'_0 \Theta_p. \quad (40)$$

We note that the approximation in (40) gets better as the pointing error variance σ_p^2 approaches zero.

Under angular pointing error, the final expression for the intensity—captured on the focal plane—becomes

$$\Lambda_s = \frac{\Lambda_0(\theta + \Theta_p)}{\sqrt{2\pi\rho^2}} \exp\left(-\frac{(x - x_0(\theta + \Theta_p))^2}{2\rho^2}\right) \cdot \mathbb{1}_A(x) \quad (41)$$

$$\begin{aligned} &\approx \left(\frac{\Lambda_0(\theta)}{\sqrt{2\pi\rho^2}} + \frac{\Lambda'_0 \Theta_p}{\sqrt{2\pi\rho^2}} \right) \\ &\quad \times \exp\left(-\frac{(x - F \sin(\theta) - F \cos(\theta)\Theta_p)^2}{2\rho^2}\right) \cdot \mathbb{1}_A(x). \end{aligned} \quad (42)$$

It is shown in the Appendix that for $|\Theta_p|$ small, Λ_s can be written (approximately) as the sum of a signal term and a noise term

$$\begin{aligned} \Lambda_s &\approx \frac{\Lambda_0(\theta)}{\sqrt{2\pi\rho^2}} \exp\left(-\frac{(x - F \sin(\theta))^2}{2\rho^2}\right) \\ &\quad + \frac{1}{\sqrt{2\pi\rho^2}} \exp\left(-\frac{(x - F \sin(\theta))^2}{2\rho^2}\right) \\ &\quad \times \left(\Lambda_0(\theta) \frac{(x - F \sin(\theta))F \cos(\theta)}{\rho^2} + \Lambda'_0 \right) \Theta_p. \end{aligned} \quad (43)$$

In (43), the first term in the sum on the right-hand side is the signal component and the second term in the sum

(containing Θ_p) is the noise component. This fact implies that the “signal” output of the m th element of the array is made of a signal term \mathcal{S}_m and a (pointing error induced) noise term, \mathcal{X}_m as

$$\Lambda_m = \int_{A_m} \Lambda_s dx \approx \mathcal{S}_m + \mathcal{X}_m \quad (44)$$

where

$$\begin{aligned} \mathcal{S}_m &:= \int_{A_m} \frac{\Lambda_0(\theta)}{\sqrt{2\pi\rho^2}} \exp\left(-\frac{(x - F \sin(\theta))^2}{2\rho^2}\right) dx \\ \mathcal{X}_m &:= \int_{A_m} \frac{1}{\sqrt{2\pi\rho^2}} \exp\left(-\frac{(x - F \sin(\theta))^2}{2\rho^2}\right) \\ &\quad \times \left(\Lambda_0(\theta) \frac{(x - F \sin(\theta))F \cos(\theta)}{\rho^2} + \Lambda'_0 \right) dx \Theta_p. \end{aligned} \quad (45)$$

Thus, the output of the m th detector of the array is given by

$$\begin{aligned} Y_m &= \Lambda_m + X_m \\ &\approx \mathcal{S}_m + Z_m \end{aligned} \quad (46)$$

where Z_m is the total noise that is the sum of two independent Gaussian random variables: X_m which represents thermal noise with variance σ_n^2 and \mathcal{X}_m which represents noise due to pointing error. The variance of \mathcal{X}_m is $\gamma_m^2 \sigma_p^2$. The constant γ_m is defined as the integral

$$\begin{aligned} \gamma_m(\theta) &:= \int_{A_m} \frac{1}{\sqrt{2\pi\rho^2}} \exp\left(-\frac{(x - F \sin(\theta))^2}{2\rho^2}\right) \\ &\quad \times \left(\Lambda_0(\theta) \frac{(x - F \sin(\theta))F \cos(\theta)}{\rho^2} + \Lambda'_0 \right) dx. \end{aligned} \quad (47)$$

The variance of Z_m , denoted by σ_m^2 , is

$$\sigma_m^2(\theta) := \gamma_m^2(\theta) \sigma_p^2 + \sigma_n^2. \quad (48)$$

Note: Here, we assume that the angle-of-arrival θ is sampled (or updated) at a frequency much slower than the frequency of the random process driving the pointing error Θ_p . The frequency at which θ is updated depends on the speed of the mobile terminal—and for most practical scenarios—the update happens on the order of a few hundreds of milliseconds. In contrast, the pointing error varies on the order of one millisecond or less. Therefore, it is safe to assume that the Gaussian noise resulting from pointing error is white for the sampling rates at which the angle-of-arrival θ is updated.

The log-likelihood function for the general receiver is given by the expression

$$\begin{aligned} \ln p(\mathbf{Y}|\theta) &= - \sum_{m=0}^{M-1} \left(\ln \left(\sqrt{2\pi\sigma_m^2} \right) + \frac{(Y_m - \mathcal{S}_m)^2}{2\sigma_m^2} \right) \\ &= - \sum_{m=0}^{M-1} \left(\ln \left(\sqrt{2\pi(\gamma_m^2(\theta)\sigma_p^2 + \sigma_n^2)} \right) + \frac{(Y_m - \mathcal{S}_m(\theta))^2}{2(\gamma_m^2(\theta)\sigma_p^2 + \sigma_n^2)} \right). \end{aligned} \quad (49)$$

It can be shown that the Fisher information of θ is

$$-\mathbb{E} \left[\frac{\partial^2 \ln p(\mathbf{Y}|\theta)}{\partial \theta^2} \right] = \sum_{m=0}^{M-1} \left(\frac{(\sigma'_m)^2}{\sigma_m^2} + \left(\frac{\sigma'_m}{\sigma_m} \right)' - \left(\frac{\sigma'_m}{\sigma_m^3} \right)' \sigma_m^2 \right) \quad (50)$$

where, through (48), $\sigma_m = \sqrt{\gamma_m^2(\theta)\sigma_p^2 + \sigma_n^2}$.

V. PERFORMANCE OF MAXIMUM LIKELIHOOD ESTIMATOR OF ANGLE OF ARRIVAL

The CRLB curves demonstrated that a smaller beamwidth provides a better angle-of-arrival estimation performance for θ close to zero, whereas a larger beamwidth provides better performance at larger values of θ . In this section, we highlight the performance of the maximum likelihood estimator of angle-of-arrival θ in terms of the mean-square error.

A. Maximum Likelihood Estimator

The maximum likelihood estimate of θ is defined as

$$\begin{aligned} \hat{\theta} &:= \arg \max_{\theta} \ln(p(\mathbf{Y}|\theta)) \\ &= \arg \max_{\theta} \left(-M \ln \left(\sqrt{2\pi\sigma_n^2} \right) - \sum_{m=0}^{M-1} \frac{(Y_m - \Lambda_m(\theta))^2}{2\sigma_n^2} \right) \\ &= \arg \max_{\theta} \left(- \sum_{m=0}^{M-1} \frac{(Y_m - \Lambda_m(\theta))^2}{2\sigma_n^2} \right) \\ &= \arg \min_{\theta} \sum_{m=0}^{M-1} \frac{(Y_m - \Lambda_m(\theta))^2}{2\sigma_n^2}. \end{aligned} \quad (51)$$

It is not straightforward to compute the maximum likelihood estimate of θ in closed form through the expression (51). Therefore, we resort to one of the numerical techniques to compute the maximum likelihood estimate. The mean-square error of the maximum likelihood estimate is computed using Monte Carlo simulations. The following method is used to estimate the mean-square error of the maximum likelihood estimator.

- 1) Generate observations by sampling the $M \times 1$ Gaussian random vector \mathbf{Y} using (22). During the sampling, the value of θ is fixed. Generate N independent vectors for a given value of θ to generate $\mathbf{Y}_1, \mathbf{Y}_2, \dots, \mathbf{Y}_N$.
- 2) Based on each observation vector \mathbf{Y}_i for $1 \leq i \leq N$, generate the maximum likelihood estimates $\hat{\theta}_i$ by numerically computing the peak of log-likelihood function $\ln(p(\mathbf{Y}_i|\theta))$ with respect to θ .
- 3) For a given value of θ , compute the mean-square error (denoted by MSE) numerically

$$\text{MSE}(\theta) := \frac{1}{N} \sum_{i=1}^N (\theta - \hat{\theta}_i)^2. \quad (52)$$

- 4) Repeat steps 1 through 3 for the next value of θ .

B. Estimation Performance Under Beamwidth Uncertainty

For long distance or mobile FSO applications, the angular beamwidth ϕ of the signal impinging on the receiver lens may not be the same as the beamwidth assumed in the model. Since the beam radius $\omega(L)$ —at a sufficiently long link distance L —is approximated by ϕL [as shown in (4)], any error in measurement of the link distance will translate to ambiguity in the value of ϕ at the receiver. This is not a serious issue in case the angle-of-arrival θ is estimated based only on the spot location. However, the relationship between the beam energy and θ depends significantly on the beamwidth ϕ , and any ambiguity in the value of ϕ can lead to performance loss while estimating the angle of arrival on the basis of spot energy. The beamwidth uncertainty problem is captured by the log-likelihood function in (51), where the measurements Y_m are driven by the actual ϕ , and the function Λ_m is computed based on $\hat{\phi}$: the assumed value of ϕ .

To understand the effect of beamwidth uncertainty on angle-of-arrival tracking, we consider the high signal-to-noise ratio regime where the effect of noise can be ignored. In this scenario, the noise variance σ_n^2 is quite small so that $Y_m \approx \Lambda_m$ for all m . Thus, the maximum likelihood estimate in (51) reduces to the following:

$$\begin{aligned} \hat{\theta} &= \arg \min_{\theta} \sum_{m=0}^{M-1} \frac{(Y_m - \Lambda_m(\theta, \hat{\phi}))^2}{2\sigma_n^2} \\ &\approx \arg \min_{\theta} \sum_{m=0}^{M-1} \frac{(\Lambda_m(\theta_0, \phi) - \Lambda_m(\theta, \hat{\phi}))^2}{2\sigma_n^2} \end{aligned} \quad (53)$$

where θ_0 is the actual angle of arrival that drives the observations. In (53), we have expressed Λ_m explicitly as a function of θ , θ_0 , ϕ , and $\hat{\phi}$. The maximum likelihood estimate of θ_0 [that will minimize (53)] is the value that will realize the equality

$$\Lambda_m(\theta_0, \phi) = \Lambda_m(\hat{\theta}, \hat{\phi}) \quad (54)$$

for each m . This implies that the maximum likelihood estimate $\hat{\theta}$, in this case, is the value of θ at which Λ_m for the assumed and the actual beamwidths become equal to each other for all m . We note the obvious fact that $\hat{\phi} = \phi \Rightarrow \hat{\theta} = \theta_0$. For the case of angle-of-arrival estimation based solely on spot energy, the beamwidth uncertainty or mismatch phenomenon is highlighted in Fig. 6, where the actual beam has a smaller beamwidth compared to the assumed model, i.e., $\hat{\phi} > \phi$. For the sake of simplicity, we only consider the case for $\theta_0 > 0$ in this figure. Here, the point of intersection is the critical value of beamwidth which is denoted by θ_c . This figure highlights the fact that for $\theta_0 < \theta_c$, the receiver underestimates the value of θ_0 , i.e., $\hat{\theta} < \theta_0$; and for $\theta_0 > \theta_c$, the receiver overestimates θ_0 : $\hat{\theta} > \theta_0$. Here, the absolute error $|\hat{\theta} - \theta_0|$ is denoted by $\tilde{\theta}$. It is straightforward to note that for the opposite case when $\hat{\phi} < \phi$, $\hat{\theta} > \theta_0$ for $\theta_0 < \theta_c$ and $\hat{\theta} < \theta_0$ for $\theta_0 > \theta_c$.

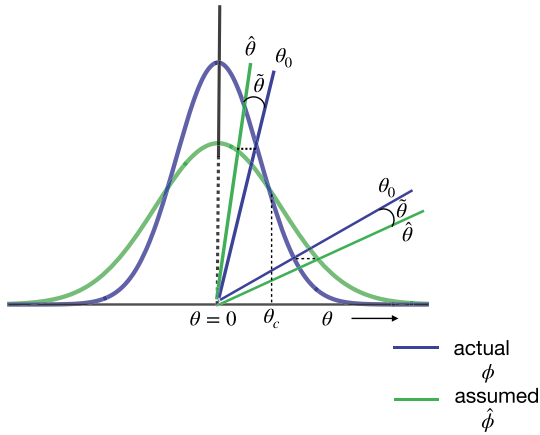


Fig. 6. Effect of beamwidth uncertainty on the angle-of-arrival estimation.

TABLE I
Default Values of System Parameters

Notation	Name / Unit	Default Values
I_0	received peak power	1 mW to 100 mW
σ_n	thermal noise standard deviation	10^{-6} Volts
θ	angle-of-arrival	$-\pi/2$ to $\pi/2$ rads
ϕ	angular beamwidth	1 to 10 mrad
L	link distance	100 to 1000 m
F	focal length	1 mm
$ \mathcal{A} $	array area	4 mm^2
ρ	spot radius	0.2 mm

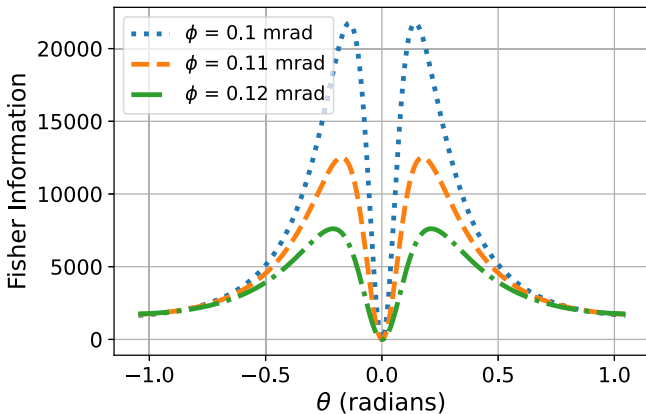


Fig. 7. Fisher information with respect to angle-of-arrival θ for different beamwidth ϕ .

VI. EXPERIMENTAL RESULTS AND DISCUSSION

In this section, we discuss experimental results conducted in this study. The default parameter values for the plots are shown in Table I.

First, we analyze and comment on the CRLB plots of angle-of-arrival θ for various channel conditions. Since the CRLB is an even function of angle-of-arrival θ , we only consider the positive θ -axis for Fig. 8 through Fig. 12.

Fig. 7 analyzes the Fisher information of θ based solely on the variation of spot energy on the focal plane (without taking into account spot location). Using (29), this Fisher

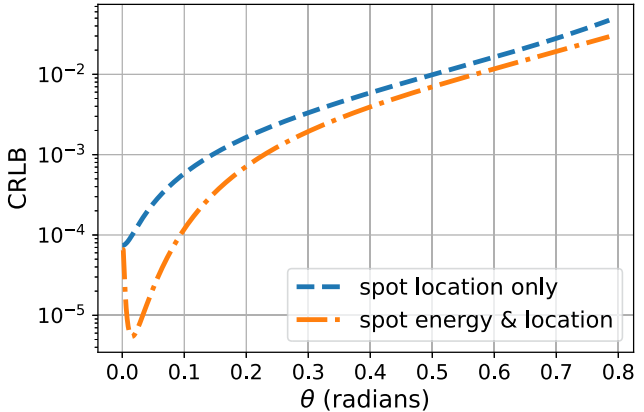


Fig. 8. Cramér–Rao lower bound comparison.

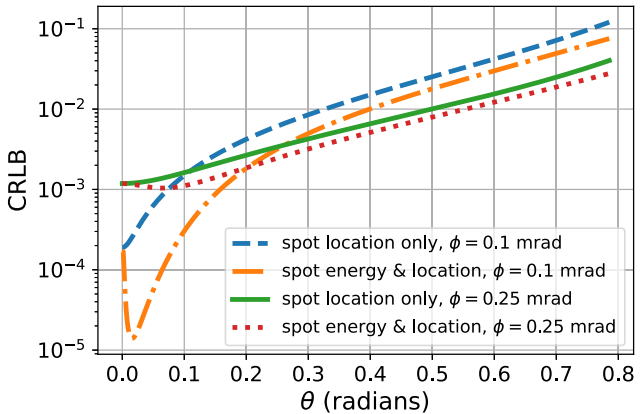


Fig. 9. Cramér–Rao lower bound comparison for different beamwidth ϕ .

information is defined by

$$-\mathbb{E} \left[\frac{\partial^2 \ln p(\mathbf{Y}|\theta)}{\partial \theta^2} \right] = \frac{1}{\sigma_n^2} \sum_{m=0}^{M-1} \alpha_m^2 \quad (55)$$

and is plotted in Fig. 7 as function of angle-of-arrival θ . We note that the Fisher information is maximized at the value of θ that corresponds to maximum rate of change of energy in the Gaussian beam as a function of θ . We also note that the Fisher information is zero at $\theta = 0$. This is because of the fact that the slope of the Gaussian intensity profile is zero when $\theta = 0$, and any small change in θ near zero does not lead to any significant changes in beam energy that can be utilized for estimating the angle of arrival with sufficient accuracy. In other words, the beam energy delivers zero information about the angle-of-arrival θ when $\theta = 0$.

Fig. 8 represents the CRLB (inverse of Fisher information) curves as a function of θ . In this figure, we compare the CRLB for two scenarios: 1) only spot location information is used to infer θ and 2) both spot energy and location are used to estimate θ . We note that the spot energy provides significant amount of information in addition to spot location that helps improve (lowers) the CRLB.

Fig. 9 depicts the CRLB curves as a function of θ for different beamwidth ϕ with the assumption that the total

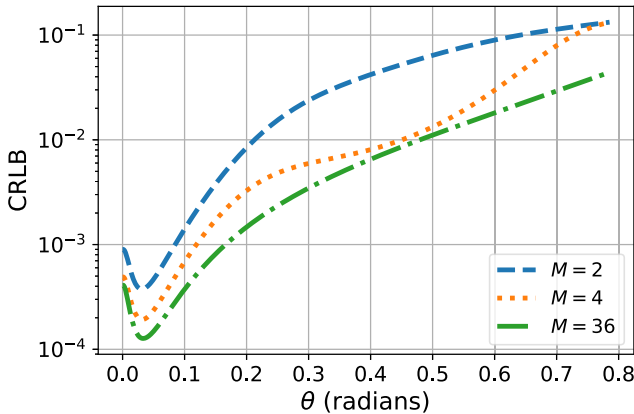


Fig. 10. Cramér–Rao lower bound comparison for different number of detectors M in the array.

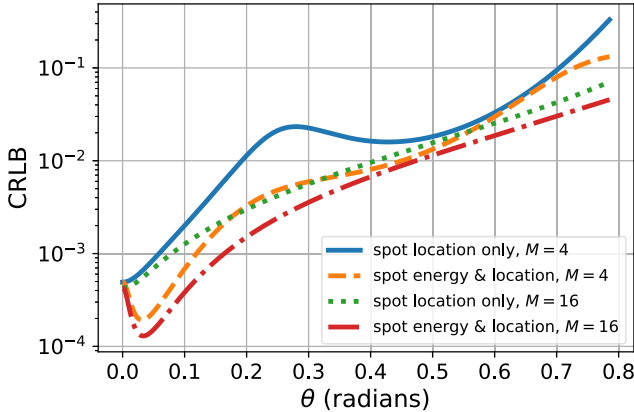


Fig. 11. Cramér–Rao lower bound comparison for different number of detectors M in the array.

energy in the beam is constant for different beamwidth values. We observe that a narrower beam leads to a smaller CRLB for smaller values of θ . However, for large values of angle-of-arrival θ , the energy of a narrow beam decays at a faster rate than a beam with a larger beamwidth, and the CRLB of a narrower beam exceeds that of a wider beam beyond a certain value of θ . Thus, depending on how quickly the angle of arrival is sampled or updated, we may want to choose the appropriate beamwidth that minimizes the CRLB. For a slow moving terminal or a high sampling rate system, we can estimate the angle of arrival more accurately with a narrow beam since θ is not varying significantly. On the other hand, for a fast moving target or a low sampling rate system, we may want to use a wider beamwidth since the deviation in θ can be large from one sampling instant to the next.

Figs. 10 and 11 represent the CRLB of θ as a function of number of detectors M . Here, we assume that the major source of noise in the receiver is due to background radiation which depends only on the active area of the detector array. For a fixed array area, a larger number of detectors yields minimization of CRLB (albeit at the cost of a higher computational complexity). We observe in Fig. 10 that the CRLB decreases monotonically as we increase the numbers

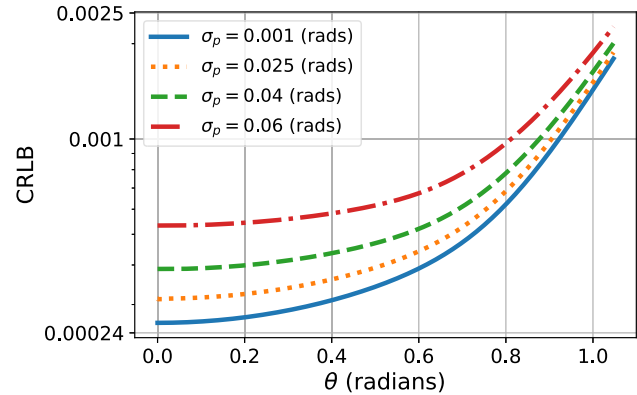


Fig. 12. Cramér–Rao lower bound comparison for different values of pointing error standard deviation σ_p .

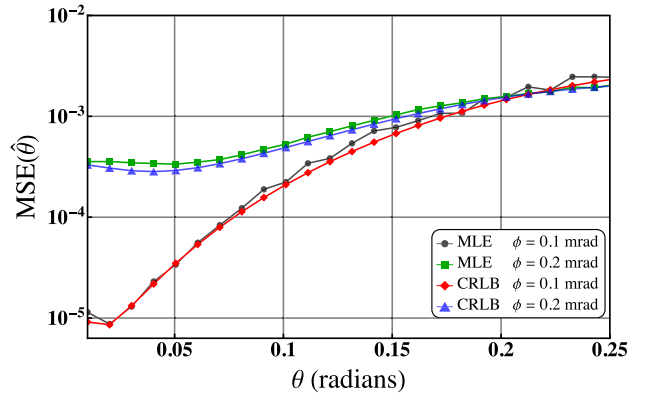


Fig. 13. Maximum likelihood estimator's MSE performance with respect to CRLB curves.

of detectors. Fig. 11 represents the CRLB based on: 1) spot location alone and 2) spot energy as well as location for two different types of detector arrays; one for the number of detectors $M = 4$ and the other for $M = 16$ (the total area of the both the arrays is the same). For small number of detectors, the CRLB curves exhibit a “wave like” effect with peaks and troughs. This is due to the fact that when the area of array is constant, a smaller number of detectors implies a larger area per detector. When the area of each detector is large compared to the spot footprint, the CRLB dips when the spot crosses over to the neighboring detector, and reaches a peak when the spot lies in the middle of the detector region [23].

Fig. 12 shows the CRLB as a function of θ for different value of pointing error standard deviation σ_p . Here, we have assumed that σ_p is only a small fraction of the angular beamwidth ϕ in order to justify small pointing error approximations made in (39), (40), and (45). The beamwidth in this set of experiments was fixed at 0.2 radians in order to account for pointing error.

Fig. 13 shows the mean-square error performance of the maximum likelihood estimator for different values of beamwidth ϕ . We have also compared the mean-square error curves with the Cramér–Rao bounds to assess the performance of the estimator.

Fig. 14 outlines the MSE of the maximum likelihood estimator under beamwidth uncertainty for different values

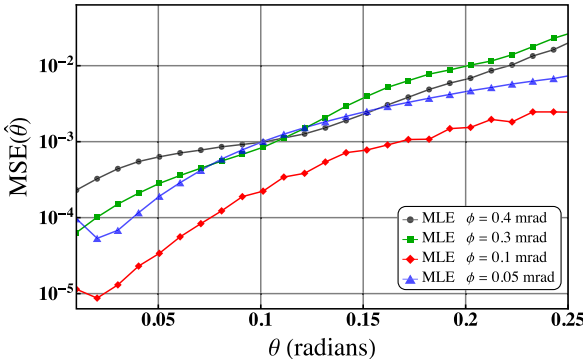


Fig. 14. Maximum likelihood estimator performance in terms of mean-square error under beamwidth mismatch.

of actual beamwidth ϕ when the assumed beamwidth $\hat{\phi}$ is fixed at 0.1 radians. We note that the beamwidth uncertainty (or model mismatch) leads to a higher MSE for the maximum likelihood estimator. However, when there is no uncertainty—i.e., the assumed and actual beamwidths $\phi = \hat{\phi} = 0.1$, as shown by the red curve—the MSE performance is optimal (lowest MSE).

VII. CONCLUSION

In this study, we proposed and showed that the angle-of-arrival θ of narrow Gaussian beams can be estimated more accurately if the variation in spot energy as a function of θ is taken into account as an extra observation in addition to the spot location on the focal plane of an optical receiver. We first established the relationship between the angle of arrival and the energy in Gaussian beam. Thereafter, we showed—through the derived CRLB plots—that significantly better estimation of angle of arrival can be achieved if spot energy is incorporated into the estimation process in addition to observations based on spot location. Depending on the beamwidth of the received Gaussian beam, the difference in performance can be significant, especially at smaller values of angle of arrival. Moreover, an accurate angle-of-arrival estimation (based on both spot energy and spot location) depends heavily on the beamwidth uncertainty: a larger beamwidth uncertainty leads to a worse mean-square error performance of the maximum likelihood estimator.

As part of a future study on this project, we want to study the dynamical problem in which the angle of arrival is assumed to evolve in time as a (Gaussian) random process. For this dynamical model, we consider applying Bayesian filtering algorithms—such as Kalman and particle filters—to track the angle of arrival. For the dynamical model, we want to quantify the improvement in tracking performance based on our proposed approach in this article.

APPENDIX

The Taylor series expansion of the exponential term in (42) is

$$\exp\left(-\frac{(x - F \sin(\theta) - F \cos(\theta)\Theta_p)^2}{2\rho^2}\right)$$

$$= \exp\left(-\frac{(x - F \sin(\theta))^2}{2\rho^2}\right) \\ \times \exp\left(\frac{2(x - F \sin(\theta))F \cos(\theta)\Theta_p}{2\rho^2}\right) \\ \times \exp\left(-\frac{F^2 \cos^2(\theta)\Theta_p^2}{2\rho^2}\right). \quad (56)$$

For $|\Theta_p| \ll 1$, we ignore the last exponential term in (56). Under this approximation and by representing the second exponential term through its first-order Taylor series approximation, we have that the intensity on the focal plane is

$$\Lambda_s \approx \exp\left(-\frac{(x - F \sin(\theta))^2}{2\rho^2}\right) \left(\frac{\Lambda_0(\theta)}{\sqrt{2\pi\rho^2}} + \frac{\Lambda'_0\Theta_p}{\sqrt{2\pi\rho^2}} \right) \\ \times \left(1 + \frac{(x - F \sin(\theta))F \cos(\theta)\Theta_p}{\rho^2} \right) \\ = \exp\left(-\frac{(x - F \sin(\theta))^2}{2\rho^2}\right) \\ \times \left(\frac{\Lambda_0(\theta)}{\sqrt{2\pi\rho^2}} + \frac{\Lambda_0(\theta)}{\sqrt{2\pi\rho^2}} \frac{(x - F \sin(\theta))F \cos(\theta)\Theta_p}{\rho^2} \right. \\ \left. + \frac{\Lambda'_0\Theta_p}{\sqrt{2\pi\rho^2}} + \frac{\Lambda'_0(x - F \sin(\theta))F \cos(\theta)\Theta_p^2}{\sqrt{2\pi\rho^6}} \right). \quad (57)$$

By ignoring the terms containing Θ_p^2 , we have that

$$\Lambda_s \approx \exp\left(-\frac{(x - F \sin(\theta))^2}{2\rho^2}\right) \frac{\Lambda_0(\theta)}{\sqrt{2\pi\rho^2}} \\ + \frac{1}{\sqrt{2\pi\rho^2}} \exp\left(-\frac{(x - F \sin(\theta))^2}{2\rho^2}\right) \\ \times \left(\Lambda_0(\theta) \frac{(x - F \sin(\theta))F \cos(\theta)}{\rho^2} + \Lambda'_0 \right) \Theta_p. \quad (58)$$

REFERENCES

- [1] A. Trichili, M. A. Cox, B. S. Ooi, and M.-S. Alouini, “Roadmap to free space optics,” *J. Opt. Soc. Amer. B*, vol. 37, no. 11, pp. A184–A201, Nov. 2020.
- [2] H. Hemmati, A. Biswas, and I. B. Djordjevic, “Deep-space optical communications: Future perspectives and applications,” *Proc. IEEE*, vol. 99, no. 11, pp. 2020–2039, Nov. 2011.
- [3] P. M. Goorjian, “Fine pointing of laser beams by using laser arrays for applications to CubeSats,” *Proc. SPIE*, vol. 11678, 2021, Art. no. 116780E.
- [4] J. S. Chang, “Small satellite optical communication receiver for simultaneous spatial tracking and data demodulation,” Master’s thesis, Massachusetts Institute of Technology, Cambridge, MA, USA, 2018.
- [5] O. Svelto and D. Hanna, *Principles of Lasers*. Berlin, Germany: Springer, 2013.
- [6] “Ericsson and PowerLight demonstrate world’s first wireless powered 5G base station,” Ericsson, Stockholm, Sweden, 2021, Accessed: Apr. 19, 2023. [Online]. Available: <https://www.ericsson.com/en/news/2021/10/ericsson-and-powerlight-achieve-base-station-wireless-charging-breakthrough>

- [7] “LaserMotive makes a switch to PowerLight and focuses on beamforming power over fiber,” GeekWire, 2017. Accessed: Apr. 19, 2023. [Online]. Available: <https://www.geekwire.com/2017/lasermotive-makes-switch-powerlight-focuses-beaming-power-fiber/>
- [8] P. D. Diamantoulakis, G. K. Karagiannidis, and Z. Ding, “Simultaneous lightwave information and power transfer,” *IEEE Trans. Green Commun. Netw.*, vol. 2, no. 3, pp. 764–773, Sep. 2018.
- [9] P. D. Diamantoulakis and G. K. Karagiannidis, “Simultaneous lightwave information and power transfer (SLIPT) for indoor IoT applications,” in *Proc. IEEE Glob. Commun. Conf.*, 2017, pp. 1–6.
- [10] P. D. Diamantoulakis, K. N. Pappi, Z. Ma, X. Lei, P. C. Sofotasios, and G. K. Karagiannidis, “Airborne radio access networks with simultaneous lightwave information and power transfer (SLIPT),” in *Proc. IEEE Glob. Commun. Conf.*, 2018, pp. 1–6.
- [11] M. S. Bashir and M.-S. Alouini, “Energy optimization of a laser-powered hovering-UAV relay in optical wireless backhaul,” *IEEE Trans. Wireless Commun.*, vol. 22, no. 5, pp. 3216–3230, May 2023.
- [12] R. Boluda-Ruiz, A. García-Zambrana, B. Castillo-Vázquez, and K. Qaraqe, “Secure communication for FSO links in the presence of eavesdropper with generic location and orientation,” *Opt. Exp.*, vol. 27, no. 23, pp. 34211–34229, Nov. 2019.
- [13] M. S. Bashir and M.-S. Alouini, “Signal acquisition with photon-counting detector arrays in free-space optical communications,” *IEEE Trans. Wireless Commun.*, vol. 19, no. 4, pp. 2181–2195, Apr. 2020.
- [14] M. S. Bashir and M.-S. Alouini, “Adaptive acquisition schemes for photon-limited free-space optical communications,” *IEEE Trans. Commun.*, vol. 69, no. 1, pp. 416–428, Jan. 2021.
- [15] Y. Kaymak, R. Rojas-Cessa, J. Feng, N. Ansari, M. Zhou, and T. Zhang, “A survey on acquisition, tracking, and pointing mechanisms for mobile free-space optical communications,” *IEEE Commun. Surveys Tut.*, vol. 20, no. 2, pp. 1104–1123, Second Quarter 2018.
- [16] R. Paschotta, *Field Guide to Lasers (Series Field Guides)*. Bellingham, WA, USA: SPIE Press, 2008.
- [17] F. Pampaloni and J. Enderlein, “Gaussian, hermite-Gaussian, and Laguerre-Gaussian beams: A primer,” 2004, *arXiv:physics/0410021v1*.
- [18] L. Mandel and E. Wolf, *Optical Coherence and Quantum Optics*. Cambridge, U.K.: Cambridge Univ. Press, 1995.
- [19] H. Safi, A. Dargahi, and J. Cheng, “Beam tracking for UAV-assisted FSO links with a four-quadrant detector,” *IEEE Commun. Lett.*, vol. 25, no. 12, pp. 3908–3912, Dec. 2021.
- [20] M. S. Bashir and M. R. Bell, “Optical beam position estimation in free-space optical communication,” *IEEE Trans. Aerosp. Electron. Syst.*, vol. 52, no. 6, pp. 2896–2905, Dec. 2016.
- [21] M. S. Bashir and M. R. Bell, “Optical beam position tracking in free-space optical communication systems,” *IEEE Trans. Aerosp. Electron. Syst.*, vol. 54, no. 2, pp. 520–536, Apr. 2018.
- [22] M. S. Bashir and M. R. Bell, “The impact of optical beam position estimation on the probability of error in free-space optical communications,” *IEEE Trans. Aerosp. Electron. Syst.*, vol. 55, no. 3, pp. 1319–1333, Jun. 2019.
- [23] M. S. Bashir, M.-C. Tsai, and M.-S. Alouini, “Cramér–Rao bounds for beam tracking with photon counting detector arrays in free-space optical communications,” *IEEE Open J. Commun. Soc.*, vol. 2, pp. 1065–1081, 2021.
- [24] J. W. Goodman, *Introduction to Fourier Optics*, vol. 1, 3rd ed., J. W. Goodman, Ed. Englewood, CO, USA: Roberts & Co Publishers, 2005.
- [25] Q. Li, S. Xu, J. Yu, L. Yan, and Y. Huang, “An improved method for the position detection of a quadrant detector for free space optical communication,” *Sensors*, vol. 19, no. 1, Jan. 2019, Art. no. 175.
- [26] M. S. Bashir and M.-S. Alouini, “Optimal power allocation between beam tracking and symbol detection channels in a free-space optical communications receiver,” *IEEE Trans. Commun.*, vol. 69, no. 11, pp. 7631–7646, Nov. 2021.
- [27] J. Želudevičius, G. Dubosas, V. Švedas, M. MilaŠevičius, and K. Regelskis, “Detection of the angle-of-arrival of an optical beam by means of interference optical filters for free-space optical communication,” *Appl. Opt.*, vol. 61, no. 24, pp. 7000–7009, Aug. 2022.
- [28] A. A. Farid and S. Hranilovic, “Outage capacity optimization for free-space optical links with pointing errors,” *J. Lightw. Technol.*, vol. 25, no. 7, pp. 1702–1710, Jul. 2007.
- [29] V. V. Mai and H. Kim, “Adaptive beam control techniques for airborne free-space optical communication systems,” *Appl. Opt.*, vol. 57, no. 26, pp. 7462–7471, Sep. 2018.
- [30] A. Bekkali, H. Fujita, and M. Hattori, “New generation free-space optical communication systems with advanced optical beam stabilizer,” *J. Lightw. Technol.*, vol. 40, no. 5, pp. 1509–1518, Mar. 2022.
- [31] M. S. Bashir and M.-S. Alouini, “Optimal positioning of hovering UAV relays for mitigation of pointing error in free-space optical communications,” *IEEE Trans. Commun.*, vol. 70, no. 11, pp. 7477–7490, Nov. 2022.
- [32] M. S. Islam, K. Shahverdi, and O. Boyraz, “Metalens integrated receiver to reduce the effect of angle of arrival jitter in free space optical communication,” *J. Opt. Soc. Amer. B*, vol. 40, no. 4, pp. 891–899, Apr. 2023.
- [33] X. Ke and Z. Tan, “Effect of angle-of-arrival fluctuation on heterodyne detection in slant atmospheric turbulence,” *Appl. Opt.*, vol. 57, no. 5, pp. 1083–1090, Feb. 2018.
- [34] H. Liu, M. S. Bashir, and M.-S. Alouini, “LiDAR-assisted acquisition of mobile airborne FSO terminals in a GPS-denied environment,” 2023, *arXiv:2304.02804*.
- [35] M. S. Bashir, “Free-space optical communications with detector arrays: A mathematical analysis,” *IEEE Trans. Aerosp. Electron. Syst.*, vol. 56, no. 2, pp. 1420–1429, Apr. 2020.
- [36] V. Vilnrotter, C.-W. Lau, M. Srinivasan, K. Andrews, and R. Mukai, “Optical array receiver for communication through atmospheric turbulence,” *J. Lightw. Technol.*, vol. 23, no. 4, pp. 1664–1675, Apr. 2005.
- [37] V. A. Vilnrotter and M. Srinivasan, “Adaptive detector arrays for optical communications receivers,” *IEEE Trans. Commun.*, vol. 50, no. 7, pp. 1091–1097, Jul. 2002.
- [38] M. Srinivasan, K. S. Andrews, W. H. Farr, and A. Wong, “Photon counting detector array algorithms for deep space optical communications,” *Proc. SPIE*, vol. 9739, 2016, Art. no. 97390X.
- [39] M. S. Bashir and S. S. Muhammad, “Time synchronization in photon-limited deep space optical communications,” *IEEE Trans. Aerosp. Electron. Syst.*, vol. 56, no. 1, pp. 30–40, Feb. 2020.
- [40] M. S. Bashir and M.-S. Alouini, “Free-space optical MISO communications with an array of detectors,” *IEEE Open J. Commun. Soc.*, vol. 1, pp. 1765–1780, 2020.
- [41] M.-C. Tsai, M. S. Bashir, and M.-S. Alouini, “Data combining schemes for a detector array receiver in free-space optical communications,” *IEEE Open J. Commun. Soc.*, vol. 3, pp. 1090–1102, 2022.
- [42] “6G: The next horizon white paper,” Huawei, Shenzhen, China, White paper, 2022. Accessed: Jun. 22, 2023. [Online]. Available: <https://www.huawei.com/en/huaweitech/future-technologies/6g-white-paper>



Ming-Cheng Tsai (Graduate Student Member, IEEE) was born in Fujian, China. He received the B.E. degree in electrical engineering from the National Taipei University of Technology, Taipei, Taiwan, in 2015, and the master’s and Ph.D. degrees from the King Abdullah University of Science and Technology, Thuwal, Saudi Arabia, in 2020 and 2023, respectively, both in electrical engineering.

From 2015 to 2018, he was a Communication Engineering Student with National Tsinghua University, Hsinchu, Taiwan. His research interests include free-space optics, signal processing for tracking systems, and estimation theory.



Muhammad Salman Bashir (Senior Member, IEEE) received the M.S. and Ph.D. degrees in electrical and computer engineering from Purdue University, West Lafayette, IN, USA, in 2014 and 2017, respectively.

He served as an Assistant Professor of Electrical Engineering with the National University of Computer and Emerging Sciences Lahore, Lahore, Pakistan, from 2017 to 2018. In 2019, he joined the Communication Theory Lab, King Abdullah University of Science and Technology, Thuwal, Saudi Arabia, as a Postdoctoral Fellow. He is currently a Lecturer (Assistant Professor) with the School of Computing and Engineering, University of Huddersfield, England, U.K. His research interests include the application of statistical signal processing, optimization and information theory for performance optimization of optical wireless communication systems.

Dr. Bashir was the recipient of the International Fulbright Science and Technology Award for his graduate studies at Purdue University. He is currently an Associate Editor for IEEE COMMUNICATION LETTERS.



Mohamed-Slim Alouini (Fellow, IEEE) was born in Tunis, Tunisia. He received the Ph.D. degree in electrical engineering from the California Institute of Technology, Pasadena, CA, USA, in 1998.

He served as a Faculty Member with the University of Minnesota, Minneapolis, MN, USA, and the Texas A&M University, Qatar, Doha, Qatar. In 2009, he joined the King Abdullah University of Science and Technology, Thuwal, Saudi Arabia, as a Professor of Electrical Engineering. His research interests include the modeling, design, and performance analysis of wireless communication systems.